

# Ab Initio Calculation of Li-Sn System: Unraveling New Phases of Superconducting Materials with Increasing Compression

Thong Leng Lim<sup>1,\*</sup>, Tiem Leong Yoon<sup>2</sup>, Yee Hui Robin Chang<sup>3</sup>, San Kiong Lai<sup>4</sup>

<sup>1</sup>Faculty of Engineering and Technology, Multimedia University, 75450 Melaka, Malaysia

<sup>2</sup>Universiti Sains Malaysia, 11800 USM, Penang, Malaysia

<sup>3</sup>Faculty of Applied Sciences, Universiti Teknologi MARA, Cawangan Sarawak, 94300 Kota Samarahan, Sarawak, Malaysia

<sup>4</sup>Complex Liquids Laboratory, Department of Physics, National Central University, Chungli 320, Taiwan

Received: 07-06-2021;

Accepted: 30-07-2021;

Published: 30-09-2021

\*Correspondence

Email: [limthongleng@gmail.com](mailto:limthongleng@gmail.com)  
(Thong Leng Lim)

© 2021 The Author(s). Published by UiTM Press. This is an open access article under the terms of the [Creative Commons Attribution 4.0 International License](#), which permits use, distribution and reproduction in any medium, provided the original work is properly cited.



## Abstract

*Stoichiometry, crystal compound, electronic attributes and superconductivity of compressed lithium-tin composites have been thoroughly studied using quantum mechanical genetic algorithm approach and the first principles computations based on density functional theory. Our simulations at moderate pressure (5-20 GPa) predict a complex convex hull diagram, with the following stable Li-rich phases: I4/mmm-Li<sub>6</sub>Sn<sub>2</sub>, P3m1-Li<sub>7</sub>Sn<sub>2</sub>, R3m-Li<sub>5</sub>Sn<sub>2</sub>, Ama2-Li<sub>4</sub>Sn<sub>2</sub>, R3m-Li<sub>5</sub>Sn<sub>2</sub>, P1-Li<sub>6</sub>Sn<sub>2</sub>, C2/m-Li<sub>4</sub>Sn<sub>1</sub>, P2<sub>1</sub>/m-Li<sub>6</sub>Sn<sub>2</sub>, P3m1-Li<sub>7</sub>Sn<sub>2</sub> and Cmcm-Li<sub>4</sub>Sn<sub>2</sub>. Careful examination at their independent elastic parameters reveals sufficient mechanical stability in them. These phases are metallic system, with reasonably high electron concentration near to Fermi level or  $N(E_F)$  that ranges from 0.6 to 2.4 states/eV cell. It is also interesting for us to observe soft modes and steep-flat energy bands at Fermi levels of Li<sub>6</sub>Sn<sub>2</sub> structures which are stable throughout the pressure range. These features are prerequisites for superconducting behavior. Linear response function with Gaussian and tetrahedron methods reveals satisfactory superconducting transition temperature  $T_c$  (3.1 ~ 6.6 K) and  $T_c$  (2.1 ~ 2.4 K), respectively. Structural transition results for based elements Li and Sn agree well with literature thus signifying reliable prediction of intermediate phases.*

## Keywords

*Density functional theory; Stable phases; Superconductivity*

## 1 Introduction

The search for materials with higher transition temperature has always been an important intent in the field of solid state. This aim is further driven by the introduction of various new procedures that are able to push the boundaries of static pressure to few hundreds GPa. Elevated pressure implicitly alters the intermolecular distances between atoms, hence influencing the stability and

promoting sequence of structural transitions through formation of different phases with higher density and symmetry. Principal parameters governing the superconducting behavior, such as electronic density of states at Fermi level and operative interaction between electrons facilitated by electron-phonon coupling, can vary when under application of external pressure. Nevertheless, not all materials are profiting from high pressure alteration. Most

superconducting metallics exhibit a decline in critical temperature ( $T_c$ ) with pressure.

In contrast, elements that are regarded as dubious superconductor may gain newfound superconducting ability when being compressed. One noteworthy interesting example is lithium, a monovalent alkali metal. One of the main advantages of lithium is its aptitude to form relatively stable intermetallic binary compounds with other elements. While early studies<sup>1,2</sup> shows that critical temperature has a direct correlation with the quantity of valence electrons per atom, diverse studies conducted thereafter indicate the existence of high  $T_c$  in pressure-induced lithium. The classic Bardeen-Cooper-Schrieffer<sup>3</sup> model proposes superconductor behavior at high temperature in components with low atomic numbers. Pseudopotential calculations carried out by Allen and Cohen<sup>4</sup> suggest evidence of superconductivity but details with regard to its transition temperature is not reported. However, several high-pressure theoretical and experiment investigations reveal that lithium only attains superconductivity at pressures exceeding 20 GPa<sup>5,6,7</sup>.

Even though the first principles calculations performed by Christensen and Novikov<sup>8</sup> forecast that  $T_c$  of a compressed face centered cubic lithium should increase dramatically with pressure, continuing raising the pressure for greater drop in resistivity is still not feasible as a study<sup>9</sup> suggests that lithium has a complex phase transition, in which it undergoes metal to semi-metal transformation when vigorously compressed. On a brighter side, recent experimental work by Matsuoka et al suggests the prevalence of superconductivity in highly pressurized Li-based alloys<sup>10</sup>. If lithium can achieve zero resistance characteristic at much lower pressure, the prospect of it remains a superconductor and survives decompression are promising since occurrence of phase reversibility during pressure drop becomes more improbable. One way to realize this is through chemical alloying by means of applying extra pressure on lithium atoms. For instance, a study<sup>11</sup> shows that addition of Si elements to hydrogen atoms causes the hydrogen-rich phase  $\text{SiH}_4$  to metalize at much lower pressure. Nevertheless, for the development of new and useful Li-based

materials, countless scientific experiments that emphasise on universal composition-structure-property maps in diverse materials' families have been conducted. This method is time consuming and often yield unsatisfactory results due to the wide range of conceivable chemistries. Other recent work on high-temperature conductivity, experimental or Ab initio work can be found in Ref.<sup>12-16</sup>.

Therefore, in this paper, we systematically investigate the possible stable and low enthalpy metastable phases of binary  $\text{Li}_x\text{Sn}_y$  via evolutionary algorithm in variable-composition mode under moderate pressures, mediated by USPEX code<sup>17,18,19</sup>. Sn is preferred because of its better electrical conductivity and large interstitial space which makes Li diffusion more favorable in it as compared to Si<sup>20,21</sup>. Our calculations unlock ten stable  $\text{Li}_x\text{Sn}_y$  phases. Electronic properties and elastic stability of each phase are studied. However, to perform and report the computationally expensive superconducting related calculations namely their electron-phonon coupling properties for all detected structures are practically not possible. We centralize our focus on the  $\text{Li}_6\text{Sn}_2$  phase which appears to be the most stable along all pressure range. Apart from widening the  $\text{Li}_x\text{Sn}_y$  system chemistry, the discovery of metallic nature in compressed Li-Sn phases also helps to enlighten us on the possible existence of pressure-induced superconductivity within these composites and will serve as a catalyst to open up the prospect of finding greater  $T_c$  at higher pressure, should actual high-pressure device that can stifle Li contamination is realized one day.

## 2 Computational Method

To identify all probable stable structures in the binary Li-Sn composites, extensive evolutionary calculations that consist of 4-8 atoms, 6-12 atoms and 8-16 atoms sample sizes were performed at pressures 5 GPa, 10 GPa and 20 GPa. When stored in high-pressure diamond anvil cells during actual experiment, efforts to maintain the purity of Li-based alloys become difficult. This could be due to the high chemical activity of Li in nature and its

reaction with diamond coatings. To make the theoretical calculations more realistic, we opted against greater pressure settings. Next, default atom dependent hard constraints such as minimum distance between atoms and minimum volume per block were accessed. In the first generation, 60 random structures with combined number of atoms per unit cell that satisfy the lower-upper limits of sample range and constraints were created. Each structure underwent five relaxation intervals, starting from unrefined to strict conditions, within the framework of density functional theory (DFT)<sup>22,23</sup> as provided by the Vienna ab initio Simulation Package (VASP)<sup>24,25</sup>. Reciprocal space resolution of Monkhorst-Pack *k*-meshes was reduced gradually from  $2\pi \times 0.15 \text{ \AA}^{-1}$  to  $2\pi \times 0.07 \text{ \AA}^{-1}$ . Methfessel and Paxton smearing with 0.2 eV width was preferred for all relaxation stages.

We used ultrasoft pseudopotentials with one and fourteen valence electrons for Li ( $2s^1$ ) and Sn ( $4d^{10}5s^25p^2$ ), respectively. Structures were selected based on fitness and those having high fitness participated in new structures formation via crossover and mutations techniques, namely the heredity (40%), random (20%), transmutation (20%), softmutation (10%) and lattice mutation (10%) operators. Addition of randomly generated compositions is imperative as it provides a diversity of structures for every generation. Softmutation refers to the induction of structural change by dislodging atoms along the softest mode eigenvectors. In lattice mutation, lattice vectors of the parent structure are changed by applying a symmetric strain matrix. This operator helps to minimize events of untimely convergence towards a particular lattice. Transmutation turns randomly chosen atoms within a parent structure into other chemical species present in it. Each newly formed offspring was again compared to preset hard restrictions, relaxed and moved into the next generation if survived. The above cycle was repeated until generation number 50. At this stage, selected low enthalpy individuals have been fully relaxed.

The calculation of the electronic properties was performed by using generalized gradient approximation (GGA)

of Perdew-Wang<sup>26</sup> furnished by VASP, in terms of exchange correlation (XC) potentials. The effects of core electrons on valence orbitals was described using projector-augmented wave approach, with plane-wave threshold kinetic energy chosen as 350 eV. Tetrahedron method with Blöchl corrections was utilized in all cases. For the computations of phonon frequencies and electron-phonon coupling (EPC) parameters, we employed Density Functional Perturbation Theory or DFPT<sup>27</sup> as implemented in the ABINIT<sup>28,29</sup> code in which norm-conserving pseudopotentials and PBE-GGA<sup>30</sup> exchange-correlation functional were preferred. To avoid having symmetric atomic positions and lattice tolerance inconsistencies that might arise due to different codes, we reoptimized every well-relaxed structure generated by VASP using ABINIT, before executing DFPT calculations. Convergence studies indicate that a cutoff of 35 Hartree and  $10 \times 10 \times 10$  *k*-point meshes were enough to produce convergence in energy. The EPC parameter was calculated by using  $5 \times 5 \times 5$  *q*-point meshes.

### 3 Results and Discussion

#### 3.1 Structural Properties

Towards the end of structural prediction, formation enthalpy ( $\Delta H_{\text{LiSn}}$ ) of the fittest structures was plotted against *y*, Sn composition. The formation enthalpy of  $\text{Li}_x\text{Sn}_y$  was evaluated by using:

$$\Delta H_{\text{LiSn}} = E_{\text{LiSn}} - [xE_{\text{Li}} + yE_{\text{Sn}}] \quad (1)$$

A specific structure is classified as energetically stable if it fulfils the following two principles: (1) being a ground state structure with negative formation enthalpy and (2) is close to the lowest lying composition. Figure 1 illustrates the convex hulls of the Li-Sn composites at surrounding pressures of 5 GPa, 10 GPa and 20 GPa. It is comprised of points that commensurate to phases with the lowest formation enthalpy at exact compositions, in reference to the lowest enthalpy structures of base elements. The perforated line joining all phases with the lowest negative formation enthalpies is

termed as convex hull. As can be seen, global minimum structures or phases with lower Gibbs free energy than any phase accumulation are tetragonal  $I4/mmm$ - $Li_6Sn_2$  at 5 GPa, trigonal  $R\bar{3}m$ - $Li_5Sn_2$  at 10 GPa and monoclinic  $P2_1/m$ - $Li_6Sn_2$  at 20 GPa. The rest of the predicted energetically competitive stoichiometries are: 1)  $P\bar{3}m1$ - $Li_7Sn_2$ ,  $R\bar{3}m$ - $Li_5Sn_2$  and  $Ama2$ - $Li_4Sn_2$  at 5 GPa, 2)  $P1$ - $Li_6Sn_2$  and  $C2/m$ - $Li_4Sn_1$  at 10 GPa and finally 3)  $P\bar{3}m1$ - $Li_7Sn_2$  and  $Cmcm$ - $Li_4Sn_2$  at 20 GPa. Their unit cell shapes, lattice parameters and Wyckoff sites are presented in Table 1-3.  $Li_6Sn_2$  at 5 GPa contains Sn atoms that occupy the octahedral O interstices whereas other geometries have Sn atoms inhabiting the tetrahedral T interstices, forming distorted structure with Li atoms. Our calculations indicate that base constituent Li undergoes transition from experimentally verified body centered cubic (bcc) to face centered cubic (fcc) at 5.0 GPa (Figure 2). The structure remains fcc up to 10.0 GPa and is consistent with findings from Olinger et al., Hanfland et al. and Struzhkin et al.<sup>31,32,33</sup>. The fcc Li transforms into tetragonal- $I422$  at 20 GPa, confirming the strong preference of compressed Li for low symmetry phases. The same figure also shows Sn changes from double bct ( $\beta$ ) structure to orthorhombic- $Imma$  at 5 GPa and finally bct- $I422$  at 20 GPa. This transition routine is also observed in other experimental works<sup>34,35,36</sup>. A consistent prediction for Li and Sn ensures the reliability of our calculations.

### 3.2 Mechanical Stability

The elastic parameters of a substance are measurable through its reaction to external stress. Contrarywise, the applied stress is mandatory in maintaining specific deformation and can be used to examine elastic properties that directly quantify the mechanical stability. The computed elastic constants for all predicted stable Li-Sn compounds are stored in Table 4. These compounds are deemed to have sufficient mechanical stability if the following stability criteria<sup>37</sup>

after being modified for elevated pressure<sup>38</sup> are satisfied.

#### Monoclinic

$$\begin{aligned}\tilde{C}_{ii} &> 0, i = 1, 2, 3, 4, 5, 6 \\ \tilde{C}_{11} + \tilde{C}_{22} + \tilde{C}_{33} + 2(\tilde{C}_{12} + \tilde{C}_{13} + \tilde{C}_{23}) &> 0 \\ \tilde{C}_{33}\tilde{C}_{55} - \tilde{C}_{35}^2 &> 0, \tilde{C}_{44}\tilde{C}_{66} - \tilde{C}_{46}^2 > 0, \tilde{C}_{22} + \tilde{C}_{33} - \tilde{C}_{23} > 0 \\ \tilde{C}_{22}(\tilde{C}_{33}\tilde{C}_{55} - \tilde{C}_{35}^2) + 2\tilde{C}_{23}\tilde{C}_{25}\tilde{C}_{35} - \tilde{C}_{23}^2\tilde{C}_{55} - \tilde{C}_{25}^2\tilde{C}_{33} &> 0\end{aligned}$$

#### Orthorhombic

$$\begin{aligned}\tilde{C}_{11} &> 0, \tilde{C}_{11}\tilde{C}_{22} > \tilde{C}_{12}^2 \\ \tilde{C}_{11}\tilde{C}_{22}\tilde{C}_{33} + 2\tilde{C}_{12}\tilde{C}_{13}\tilde{C}_{23} - \tilde{C}_{11}\tilde{C}_{23}^2 - \tilde{C}_{22}\tilde{C}_{13}^2 - \tilde{C}_{33}\tilde{C}_{12}^2 &> 0 \\ \tilde{C}_{44} &> 0, \tilde{C}_{55} > 0, \tilde{C}_{66} > 0\end{aligned}$$

#### Tetragonal

$$\tilde{C}_{11} > |\tilde{C}_{12}|, 2\tilde{C}_{13}^2 < \tilde{C}_{33}(\tilde{C}_{11} + \tilde{C}_{12}), \tilde{C}_{44} > 0, \tilde{C}_{66} > 0$$

#### Trigonal

$$\begin{aligned}\tilde{C}_{11} &> |\tilde{C}_{12}|, 2\tilde{C}_{13}^2 < \tilde{C}_{33}(\tilde{C}_{11} + \tilde{C}_{12}), \tilde{C}_{44} > 0 \\ 2(\tilde{C}_{14}^2 + \tilde{C}_{15}^2) &< \tilde{C}_{44}(\tilde{C}_{11} - \tilde{C}_{12})\end{aligned}$$

where for all classes

$$\begin{aligned}\tilde{C}_{ii} &= C_{ii} - P, \tilde{C}_{ij} = C_{ij} \text{ for } i = 1, 2, 3 \text{ and } j = 4, 5, 6 \\ \tilde{C}_{12} &= C_{12} + P, \tilde{C}_{13} = C_{13} + P, \tilde{C}_{23} = C_{23} + P \\ \tilde{C}_{45} &= C_{45}, \tilde{C}_{46} = C_{46}, \tilde{C}_{56} = C_{56}\end{aligned}$$

By substituting the elastic parameters in Table 4 into the above corresponding inequalities, we noticed that all predicted phases satisfy the stability requirements, hence confirming sufficient mechanical stability in each of them. The high compressibility in x, y and z directions suggests the presence of ionic bonding

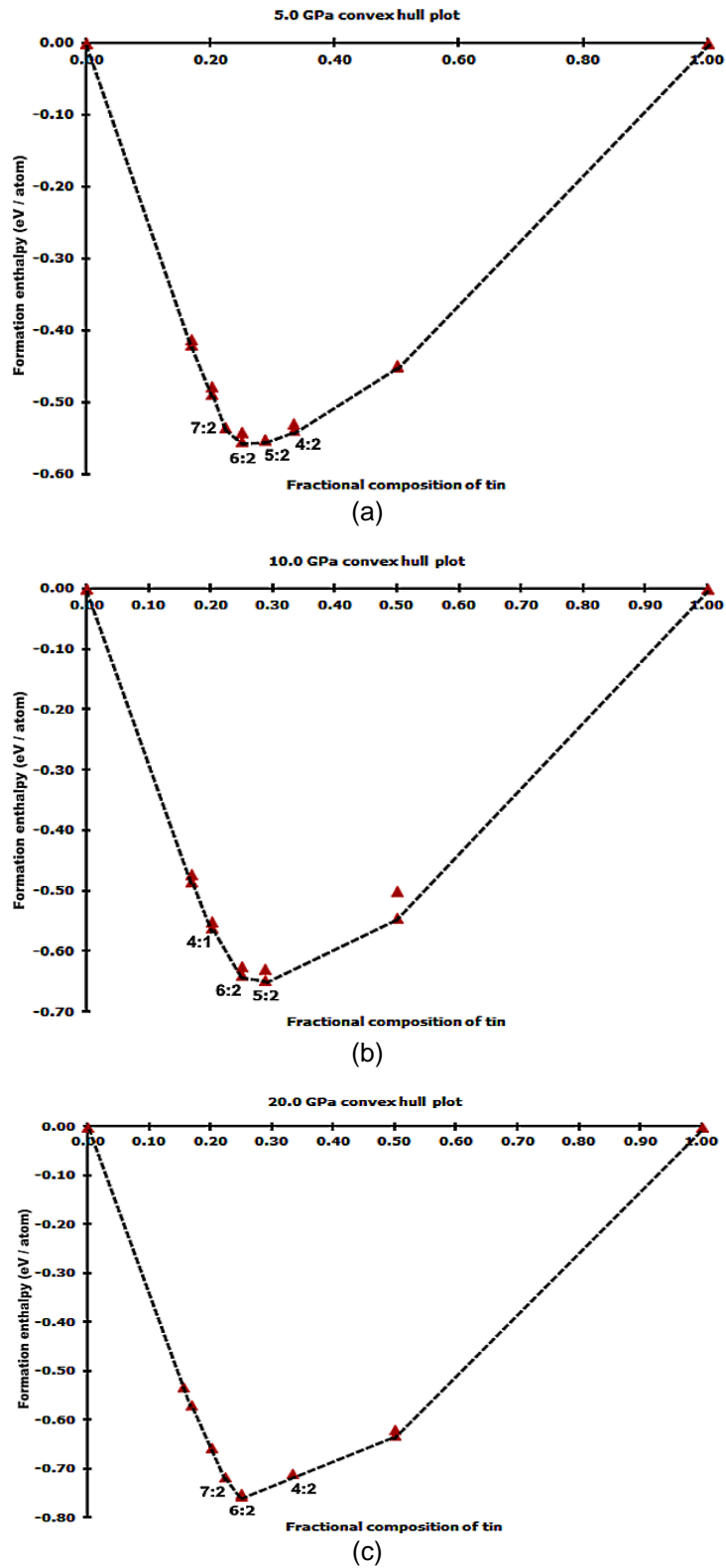


Figure 1. Formation enthalpy per block as a function of  $y$  for  $\text{Li}_x\text{Sn}_y$  system at a) 5 GPa, b) 10 GPa and c) 20 GPa

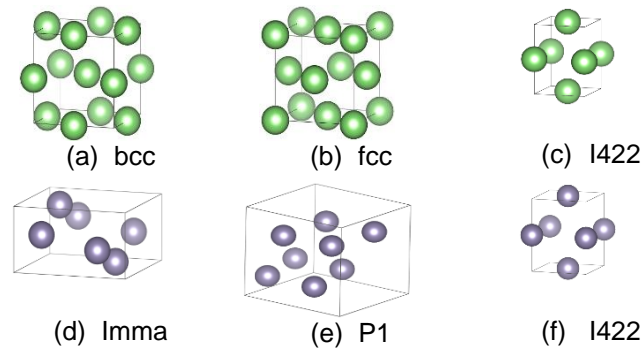


Figure 2. Li crystal at a) 5.0 GPa, b) 10.0 GPa and c) 20.0 GPa, followed by Sn structure at d) 5.0 GPa, e) 10.0 GPa and f) 20.0 GPa

Table 1. Crystallographic data of fit  $\text{Li}_x\text{Sn}_y$  alloys at 5 GPa

Phase	Unit cell	Lattice constants / Å			Atomic Wyckoff positions
		a	b	c	
$\text{Li}_7\text{Sn}_2$		4.323	4.323	7.928	Li 2d (0.3333, 0.6667, -0.4248) Li 2d (0.3333, 0.6667, -0.1020) Li 2c (0.0000, 0.0000, -0.3301) Li 1a (0.0000, 0.0000, 0.0000) Sn 2d (0.3333, 0.6667, 0.2366)
$\text{Li}_6\text{Sn}_2$		4.291	4.291	6.253	Li 2a (0.0000, 0.0000, 0.0000) Li 4d (0.0000, 0.5000, 0.2500) Sn 2b (0.0000, 0.0000, 0.5000)
$\text{Li}_5\text{Sn}_2$		4.377	4.377	18.675	Li 3a (0.0000, 0.0000, 0.0000) Li 6c (0.0000, 0.0000, -0.1502) Li 6c (0.0000, 0.0000, 0.2878) Sn 6c (0.0000, 0.0000, -0.4256)
$\text{Li}_4\text{Sn}_2$		4.401	14.756	2.927	Li 4b (0.2500, 0.2211, 0.2255) Li 4b (0.2500, -0.4478, 0.3004) Sn 4b (0.2500, 0.3846, -0.1942)



Table 2. Crystallographic data of fit  $\text{Li}_x\text{Sn}_y$  alloys at 10 GPa

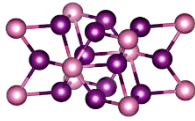
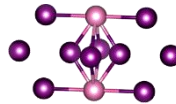
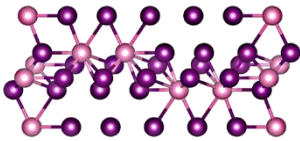
$\text{Li}_4\text{Sn}_1$		7.249	4.317	4.702	Li 4i (−0.3954, 0.0000, 0.1965) Li 4i (0.2099, 0.0000, 0.3708) Sn 2a (0.0000, 0.0000, 0.0000)
$\text{Li}_6\text{Sn}_2$		7.270	4.207	4.187	Li 2i (−0.1227, 0.1215, −0.1266) Li 1d (0.5000, 0.0000, 0.0000) Li 2i (−0.3773, 0.3816, −0.3731) Li 1g (0.0000, 0.5000, 0.5000) Sn 2i (−0.2500, −0.2483, 0.2502)
$\text{Li}_5\text{Sn}_2$		4.232	4.232	18.356	Li 6c (0.0000, 0.0000, 0.2124) Li 6c (0.0000, 0.0000, −0.3496) Li 3b (0.0000, 0.0000, 0.5000) Sn 6c (0.0000, 0.0000, 0.0756)

Table 3. Crystallographic data of fit  $\text{Li}_x\text{Sn}_y$  alloys at 20 GPa

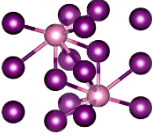
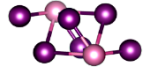
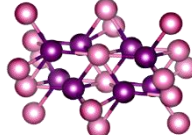
$\text{Li}_7\text{Sn}_2$		4.076	4.076	7.302	Li 1b (0.0000, 0.0000, 0.5000) Li 2c (0.0000, 0.0000, 0.1603) Li 2d (0.3333, 0.6667, −0.0807) Li 2d (0.3333, 0.6667, −0.3969) Sn 2d (0.3333, 0.6667, 0.2627)
$\text{Li}_6\text{Sn}_2$		4.045	5.776	4.029	Li 4f (0.2486, −0.0006, 0.2537) Li 2e (−0.2513, 0.2500, 0.2469) Sn 2e (0.2514, 0.2500, −0.2465)
$\text{Li}_4\text{Sn}_2$		8.088	4.393	4.382	Li 8g (−0.1748, 0.2051, 0.2500) Sn 4c (0.0000, −0.2844, 0.2500)

Table 4. Elastic constants (GPa) for stable phases within Li-Sn alloys at specific pressure

$C_{ij}$	5 GPa				10 GPa			20 GPa		
	$\text{Li}_7\text{Sn}_2$	$\text{Li}_6\text{Sn}_2$	$\text{Li}_5\text{Sn}_2$	$\text{Li}_4\text{Sn}_2$	$\text{Li}_4\text{Sn}_1$	$\text{Li}_6\text{Sn}_2$	$\text{Li}_5\text{Sn}_2$	$\text{Li}_7\text{Sn}_2$	$\text{Li}_6\text{Sn}_2$	$\text{Li}_4\text{Sn}_2$
$C_{11}$	112.95	113.17	164.58	142.78	137.99	145.52	147.65	190.25	187.66	189.77
$C_{12}$	30.35	26.76	2.07	16.86	22.24	20.16	30.94	55.46	9.86	41.56
$C_{13}$	14.70	15.34	30.65	27.75	16.47	28.53	16.71	20.37	72.61	60.30
$C_{22}$	118.78	118.94	118.35	106.67	138.75	148.11	150.13	178.26	186.78	194.64
$C_{23}$	8.23	12.85	34.81	28.64	31.99	28.14	12.78	31.41	75.60	44.52
$C_{33}$	126.29	130.73	94.41	110.96	142.95	141.77	213.53	205.50	119.70	180.64
$C_{44}$	30.31	29.13	60.15	42.66	60.79	45.02	42.11	53.61	93.49	71.82
$C_{55}$	35.31	32.38	56.99	42.57	24.89	45.17	47.94	42.85	91.31	71.20
$C_{66}$	44.57	43.12	28.25	35.01	31.43	37.47	58.08	70.45	27.71	68.02

### 3.3 Electronic Properties

Having examined the primitive cells and energetics of numerous  $\text{Li}_x\text{Sn}_y$  stoichiometries, we now shift to their electronic properties. Figure 3 shows the total and projected density of states (PDOS) for all ground-state composites. It is clearly depicted that their respective PDOS are made up of three pronounced energy regions: (1) a deep lying valence band, (2) an overlapped Sn-*p*/Li-*p* band and (3) a moderately filled higher lying Li-*p* band. The first band is subjugated by the Sn-*s* orbitals with diminutive contribution from *s* and *p* orbitals of Li atoms. Hence, the influence of this band to the bonding is fairly scarce. Subsequent upper valence band is a result of hybridization from the *p* states of Sn and Li atoms. The Li-sites in this region possess sturdily mixed *s* and *p* characters, demonstrating that the local density of states or DOS originates from extended states centered at the Sn atoms and trespass into the Li spheres. Covalency is enhanced under these circumstances. This bonding is also responsible for the non-zero DOS mark at Fermi level, indicating metallic behavior. There are however few Li-*s* and Sn-*s* in the Fermi level vicinity, inferring pressure induced charge transfer from *s* to *p* and *d* electrons. The pressure-stimulated  $s \rightarrow p, d$  charge transfer promotes thermodynamic stability, as revealed in Figure 2 whereby the higher-pressure phases possess lower formation enthalpy. The large electronic DOS at Fermi level, noted in all phases, represents a high tendency of electron-phonon interaction. As suggested by the following electron-phonon coupling ( $\lambda$ ) relationship<sup>39</sup>,

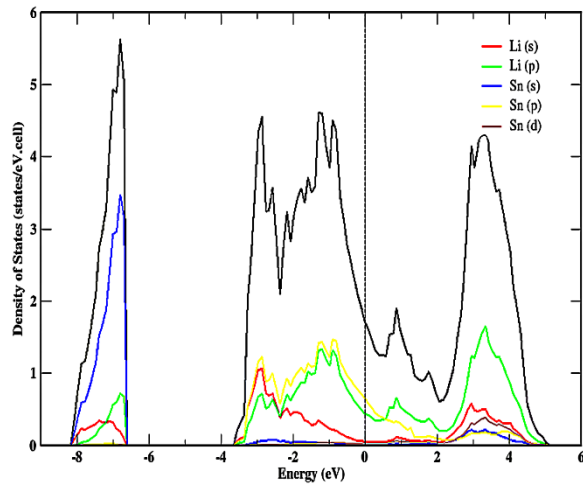
$$\lambda = \frac{N(E_F)\langle f^2 \rangle}{M\langle \omega^2 \rangle} \quad (2)$$

where the numerator (element of electron-ion over Fermi sea) is the electronic contributions while denominator (product of ion mass and average phonon frequency squared) denotes lattice vibration terms, a large electronic density at Fermi level is essential to superconducting trait. Meticulous examination illustrates that these phases have electronic DOS at

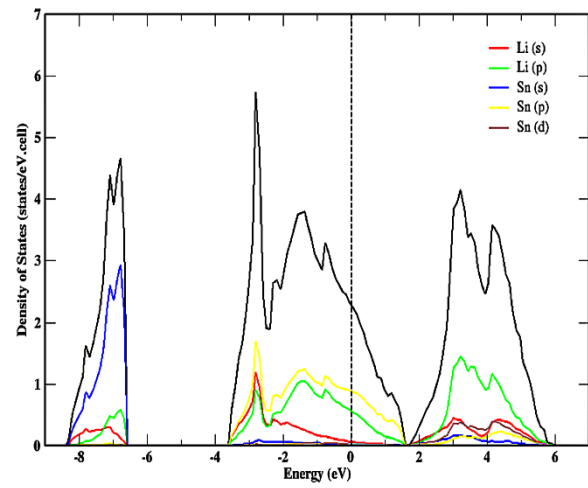
Fermi energy ranging between 0.6-2.4 states/eV per formula unit. Monotonic relationship between  $N(E_F)$  marks and Li or Sn compositions is not evident. Comparatively,  $\text{Li}_6\text{Sn}_2$  phases display higher  $N(E_F)$ .

Let us now move to the upper most band. It can be depicted that this region is largely occupied by the bonding *p* orbitals of Li atoms. Vacant antibonding Sn-*d*/Li-*p* and antibonding Sn-*d*/Li-*s* states occupy the bottom section of the conduction band. These outcomes point to the existence of mixed mild covalent Sn-Li and metallic Li-Li bonding nature in our predicted Li-Sn alloys. When comparing identical stoichiometry at different pressures, band widths of higher pressure phases appear greater. This signifies improvement in structural stability due to enhanced electrons delocalization in which additional electrons take part in bonding formations. However, the better bonding interactions at elevated pressure come at the expense of  $N(E_F)$ , a consequence of overall bands broadening. The presence of staircase feature is not seen in all DOS plots, thus indicating incompatibility of compressed LiSn phases as two-dimensional materials. Another notable common and striking feature favoring superconductivity is the appearance of pseudogap or valley near Fermi level. The states depression is formed as a result of energy usage in breaking Cooper pairs, a combining form of electron duos that arose from ion-lattice reciprocation. For  $\text{Li}_6\text{Sn}_2$ , the occurrence of multiple steep and flat bands crossing the Fermi level (see Figure 4) is a promising condition for the enhancement of electron-phonon coupling. Though a necessity, this appearance does not guarantee sufficient superconducting activity and can only be confirmed through electron-phonon calculations. Another interesting attribute is the intersection of two nearly parallel bands. This phenomenon is a sign of plausible Fermi surface nesting and may lead to manifestation of superconductivity order.

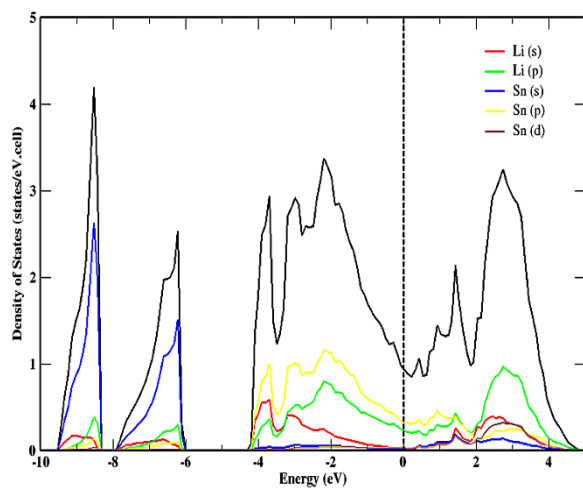




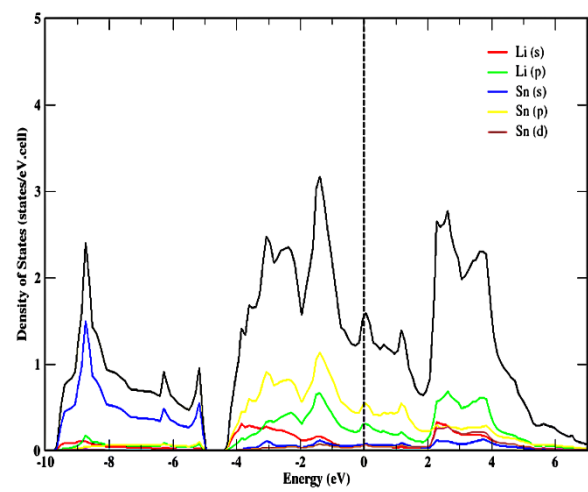
(a)  $\text{Li}_7\text{Sn}_2$



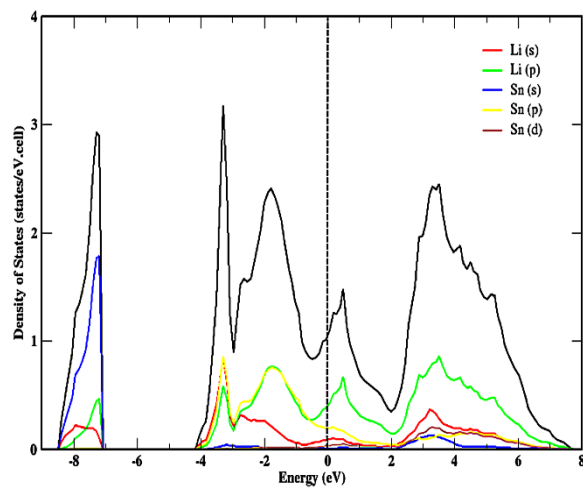
(b)  $\text{Li}_6\text{Sn}_2$



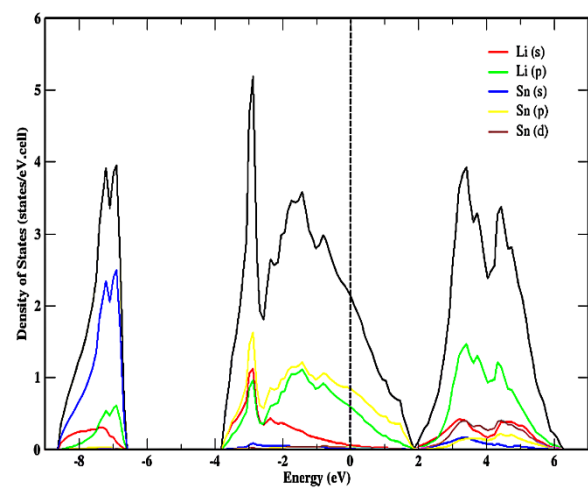
(c)  $\text{Li}_5\text{Sn}_2$



(d)  $\text{Li}_4\text{Sn}_2$



(e)  $\text{Li}_4\text{Sn}_1$



(f)  $\text{Li}_6\text{Sn}_2$

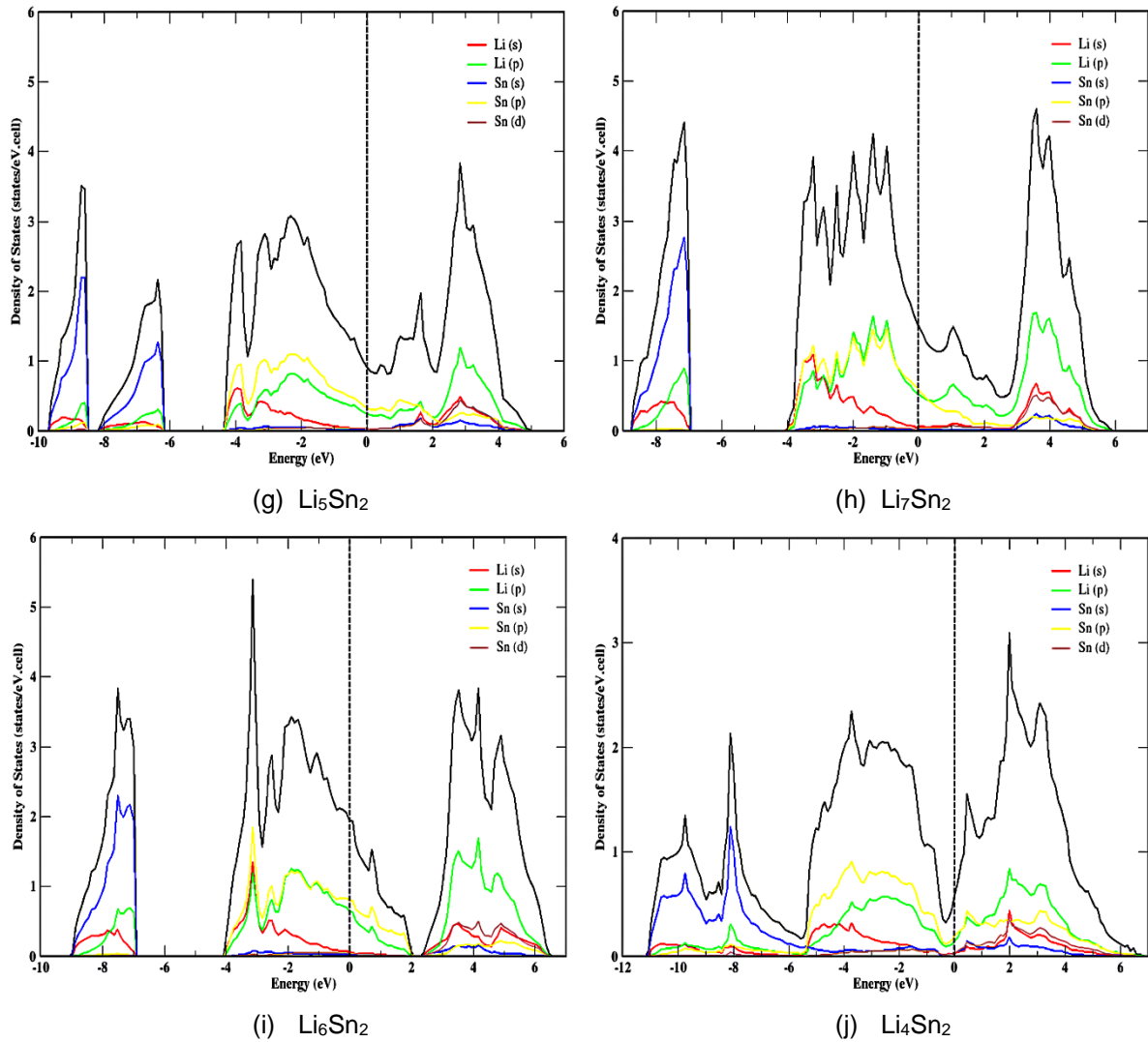


Figure 3. The total and partial density of states (PDOS): (a) – (d) at 5 GPa, (e) – (g) at 10 GPa and (h) – (j) at 20 GPa. Vertical perforated line denotes Fermi level.

### 3.4 Superconductive Properties

Phonon spectra of  $\text{Li}_6\text{Sn}_2$  -  $I4/mmm$ , and  $P2_1/m$  at three different pressures are plotted (see Figure 5). Nonappearance of imaginary frequency in the entire Brillouin zone is observed for  $\text{Li}_6\text{Sn}_2$  at 5 GPa and 10 GPa thus ensuring dynamical stability in these phases. As for  $\text{Li}_6\text{Sn}_2$  at 20 GPa, one of its acoustic modes is negative. The imaginary frequency along E-A and A-X infers that the monoclinic  $P2_1/m$  structure is unstable with respect to long wavelength modulations. Our calculated Voigt and

Reuss bulk modulus for  $P2_1/m$  at this pressure is nonetheless positive, whereby  $B_V$  and  $B_R$  are 90.03 GPa and 90.01 GPa respectively. As such,  $P2_1/m$  is stable under uniform compression. The much heftier and mildly bonded Sn atoms dominate the low-frequency region while vibration of Li atoms makes up the middle-high frequency areas. As expected, elevation of pressure raises the peak of top-lying optical modes and narrows the gap between successive regions. Soft modes associated with triply and doubly degenerate phonons are noted in all  $\text{Li}_6\text{Sn}_2$  phases.

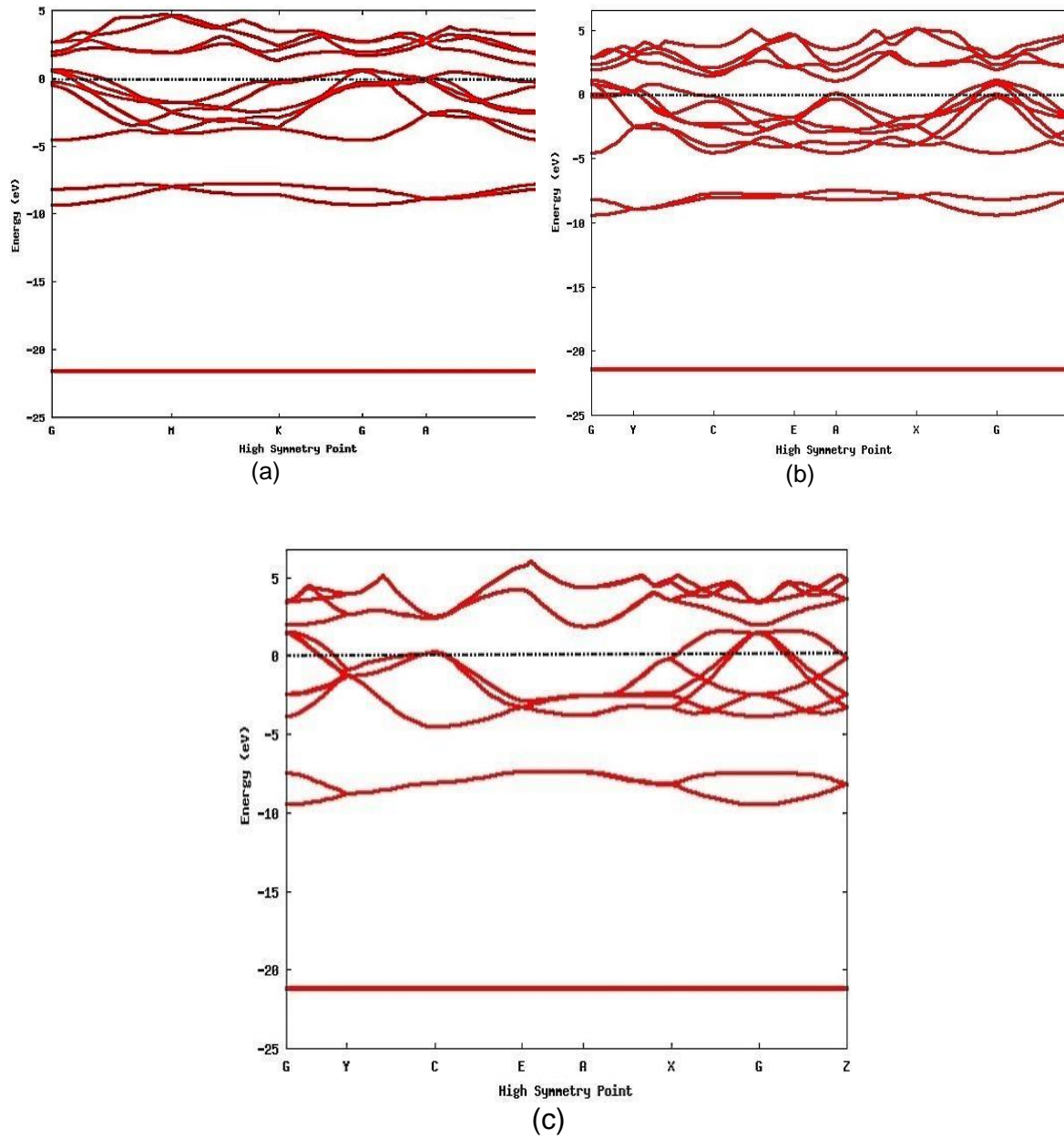


Figure 4. Band structure plots for Li<sub>6</sub>Sn<sub>2</sub> at 5, 10 and 20 GPa. Horizontal dashed line indicates Fermi level

The formation of soft modes along peculiar high-symmetry line direction serves as evidence of considerable electron-phonon coupling interactions. BCS model theory is capable of describing in detail the phenomenology of superconductivity. However, it lacks predictive power. When it is applied to actual materials study, couplings and  $T_c$  are fitted to the experimental value. The essential kind of correlation in superconductivity is the one between electrons and holes. This creates the phase space in which the pairing interaction can scatter the cooper pairs.

Description of such interaction can be achieved using a combination of complex Hamiltonian and both normal plus anomalous states Green's functions, solved via DFPT. The critical temperature is computable via Eliashberg relationship<sup>40</sup>. This equation is linked to an approach used by Frohlich<sup>41</sup> which proposed an isotropic model defined by the complex Hamiltonian

$$\hat{H} = \hat{H}_e + \hat{H}_{ph} + \sum_{j, k, q} g_{k+q, k}^{j, q} \hat{a}_{k+q}^\dagger \hat{a}_k (\hat{b}_{-q, j}^\dagger + \hat{b}_{q, j}) \quad (3)$$

where  $\hat{a}_k^+$ ,  $\hat{a}_k$ ,  $\hat{b}_j^+$  and  $\hat{b}_j$  are the annihilation and creation operators of electrons and phonons respectively. Term  $q$  denotes the phonon momentum. Addition of a perturbed Hamiltonian (given by the phonon field and Coulomb interaction between electrons) to  $\hat{H}$  Kohn-Sham Hamiltonian gives rise to the interacting Green's function associated to the perturbed Hamiltonian is expressible in terms of irreducible self energy  $\bar{\Sigma}$ , forming the following Dyson equation:

$$\bar{\Sigma}(i\omega, k) = [\bar{G}_0(i\omega, k)]^{-1} - [\bar{G}(i\omega, k)]^{-1} \quad (4)$$

Expanding  $\bar{\Sigma}$  and considering only the first terms of the expansion will lead to Eliashberg equations. These equations can be solved via series of frequentative self-consistent scheme. Matrix element of electron-phonon interaction  $g_{k+q, k}^{j, q}$  can be calculated within the harmonic approximation implemented in ABINIT through:

$$g_{k+q, k}^{j, q} = \sqrt{\frac{\hbar}{2M\omega_{qj}}} \int \psi_k^*(r) \left[ \frac{dV_{scf}}{du_q} \times \frac{u_q}{|u_q|} \right] \psi_{k+q}(r) d^3r \quad (5)$$

in which  $u_q$  represents the displacement of atom of mass  $M$  in the  $q, j$  phonon mode. The calculated Eliashberg spectral function  $\alpha^2F(\omega)$  was plotted and positioned adjacent to its corresponding phonon dispersion curves in Figure 5. The same figure shows that the coupling between electrons, wagging resonance and stretching vibrations of Li is pivotal to superconductivity, contributing to more than 60% of EPC parameter. Low-frequency translational modes of Sn atoms have a lesser contribution that expands with further compression. Computed  $\lambda$ ,  $\omega_{log}$  and  $T_c$  for I4/mmm, P1

and P2<sub>1</sub>/m structures are listed in Table 5. Gaussian smearing and tetrahedron method for  $k$ -space integration at Fermi surface were considered. The superconducting transition temperature was estimated by using the following Allen-Dynes modified McMillan<sup>42</sup> relationship:

$$T_c = \frac{\omega_{log}}{1.2} \exp \left[ -\frac{1.04(1+\lambda)}{\lambda - \mu^*(1+0.62\lambda)} \right] \quad (6)$$

where

$$\lambda = 2 \int_0^\infty \frac{\alpha^2F(\omega)}{\omega} d\omega \quad (7)$$

is the EPC constant,

$$\omega_{log} = \exp \left( \frac{2}{\lambda} \int_0^\infty \log \omega \frac{\alpha^2F(\omega)}{\omega} d\omega \right) \quad (8)$$

is the logarithmic average frequency and  $\mu^*$  denotes the screened Coulomb pseudopotential. The value of  $\mu^*$  reacts strongly with surrounding condition. The effect of local-field causes it to decline, while the effect of exchange-correlation on electron dielectric screening raises it significantly. These make the exact estimation of  $\mu^*$  highly devastating. For brevity and reliability,  $\mu^* = 0.1$  was applied in our simulations. The reliability of this value is validated by Morel et al.<sup>43</sup> in their work concerning the calculation of superconducting state parameters, in which  $\mu^*$  is practically 0.1 for most metals ranging from Group 1 to 14, including a number of the first three rows of transition elements<sup>43</sup>. As pressure increases from 5 GPa to 10 GPa,  $T_c$  displays a decreasing trend, accompanied by opposite swing between  $\omega_{log}$  and  $\lambda$ . Although coupling strength increases significantly at 20 GPa,  $T_c$  continues to drop as the severely low  $\omega_{log}$  fails to compensate  $\lambda$ .

Table 5 Calculated electron-phonon parameter  $\lambda$ , logarithmic average phonon frequency  $\omega_{log}$  (K) and transition temperature  $T_c$  (K)

Phase	Pressure (GPa)	Gaussian smearing			Tetrahedron method		
		$\lambda$	$\omega_{log}$	$T_c$	$\lambda$	$\omega_{log}$	$T_c$
Li <sub>6</sub> Sn <sub>2</sub>	5	0.773	150.36	6.556	0.528	160.88	2.410
	10	0.703	150.65	5.301	0.507	168.58	2.164
	20	1.533	26.38	3.069	1.116	25.47	2.077

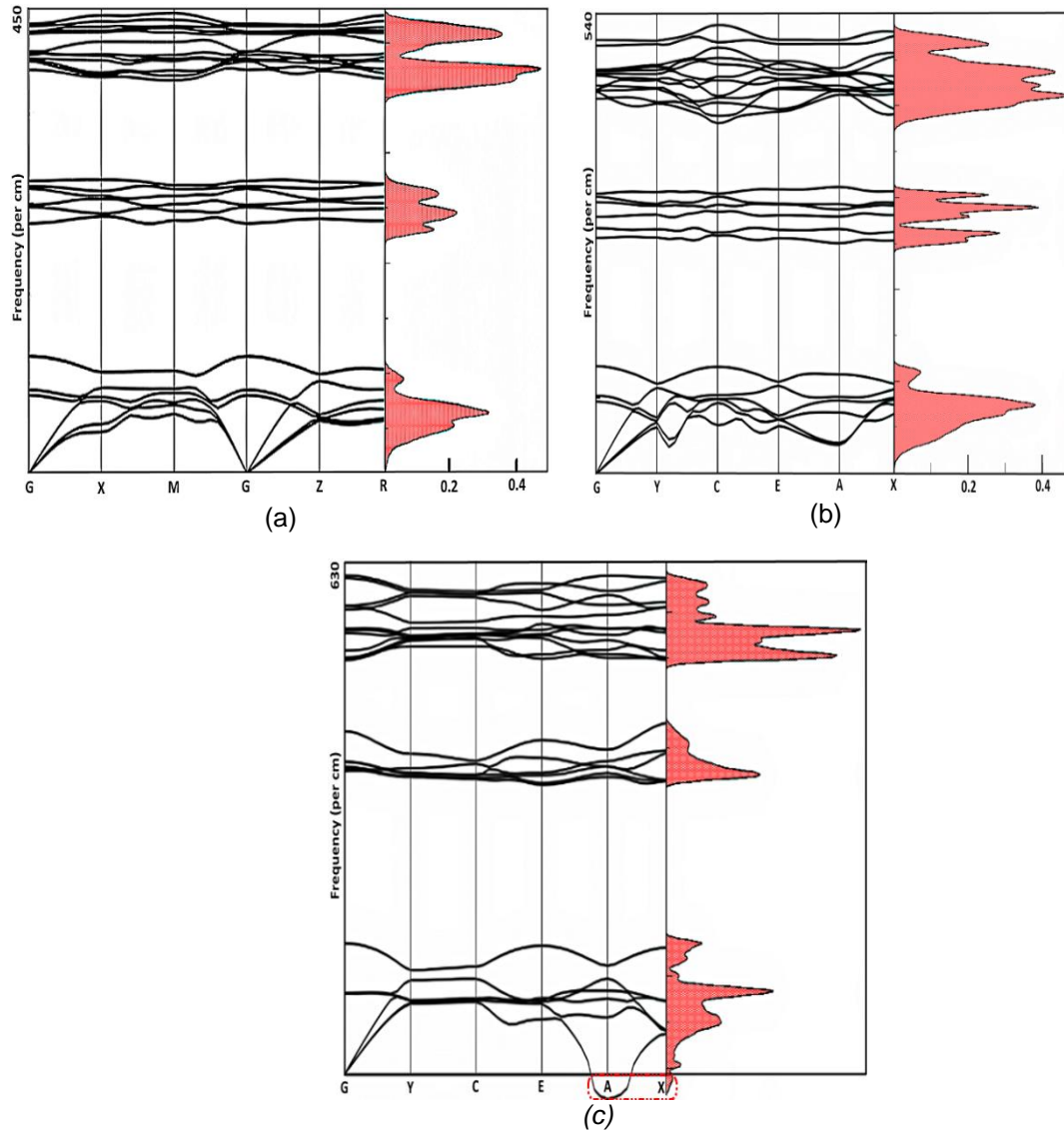


Figure 5. Computed phonon spectra and Eliashberg function  $\alpha^2F(\omega)$  for  $\text{Li}_6\text{Sn}_2$  at (a) 5 GPa, (b) 10 GPa and (c) 20 GPa

Since  $\text{Li}_6\text{Sn}_2$  at 20 GPa demonstrates an abrupt decrease of  $\omega_{\log}$  from 160 (10 GPa) to around 25, further calculations are needed to probe the possibility of having erroneous  $\lambda$  and  $\omega_{\log}$  values. As such, we have computed the dimensionless ratio  $2\Delta(0)/k_B T_c$  for  $\text{Li}_6\text{Sn}_2$  at 20 GPa by using

$$\frac{2\Delta(0)}{k_B T_c} = 3.53 \left[ 1 + 12.5 \left( \frac{T_c}{\omega_{\log}} \right)^2 \ln \left( \frac{\omega_{\log}}{2T_c} \right) \right] \quad (9)$$

whereby  $\Delta(0)$  and  $k_B$  are the zero-temperature gap edge and Boltzmann constant respectively. In BCS theory, this fraction equals to a constant value of 3.53 but within Eliashberg framework, it has a lower bound value of 3.53 and increases as

$\lambda$  rises. From Table 5, we obtained dimensionless ratio of 4.40 (Gaussian smearing) and 4.06 (Tetrahedron method). These values are consistent with the findings by Mitrović et al.<sup>44</sup>.

## Conclusion

The combination of variable composition screening and the first principles techniques have unlocked ten energetically stable  $\text{Li}_x\text{Sn}_y$  phases at low-moderate pressure. These phases possess sufficient preliminary mechanical stability as indicated by the true inequality statements when substituting their respective elastic constant into the obligatory stability criteria. High electronic

density of states at Fermi level are also noted in these phases. In addition,  $\text{Li}_6\text{Sn}_2$  crystals have soft phonon modes and possible nesting of two Fermi surfaces. The electron-phonon coupling strength of predicted  $\text{Li}_6\text{Sn}_2$  structures is largely derived from Li vibration modes. Both Gaussian and tetrahedron methods produce a moderate  $T_c$  that declines with increasing pressure. The present theoretical study is expected to provide a better understanding of the pressure-induced transitions and characterization of Li-Sn alloys under moderate compression.

### Conflict of Interest

The authors report no financial or any other conflicts of interest in this work.

### Acknowledgement

We gratefully acknowledge the Agency for Science, Technology and Research, Singapore, for providing us with the computing resources to carry out part of the calculations shown in this study.

### References

- Matthias, B. T. (1953). Transition temperatures of superconductors. *Physical Review*, 92(4), 874-876.
- Matthias, B. T. (1955). Empirical relation between superconductivity and the number of valence electrons per atom. *Physical Review*, 97(1), 74-76.
- Bardeen, J., Cooper, L. N., & J. R. Schrieffer. (1957). Theory of superconductivity. *Physical Review*, 108(5), 1175-1204.
- Allen, P. B., & Cohen, M. L. (1969). Pseudopotential calculation of the mass enhancement and superconducting transition temperature of simple metals. *Physical Review*, 187(2), 525-538.
- Shimizu, K., Ishikawa, H., Takao, D., Yagi, T., & Amaya, K. (2002). Superconductivity in compressed lithium at 20 K, *Nature*, 419(6907), 597-599.
- Struzhkin, V., Eremets, M. I., Gan, W., Mao, H. K., & Hemley, R. J. (2002). Superconductivity in dense lithium, *Science*, 298(5596), 1213-1215.
- Deemyad, S., & Schilling, J. S. (2003). Superconducting phase diagram of Li metal in nearly hydrostatic pressures up to 67 GPa, *Physical Review Letters*, 91(16), 167001.
- Christensen, N. E., & Novikov, D. L. (2001). Predicted superconductive properties of lithium under pressure, *Physical Review Letters*, 86(9), 1861-1864.
- Matsuoka, T. & Shimizu, K. (2009). Direct observation of a pressure-induced metal-to-semiconductor transition in lithium, *Nature Letters*, 458(7235), 186-189.
- Matsuoka, T., Kuno, K., Ohta, K., Sakata, M., Nakamoto, Y., Hirao, N., Ohishi, Y., Shimizu, K., Kume, T., & Sasaki, S. (2017). Lithium polyhydrides synthesized under high pressure and high temperature, *Journal of Raman Spectroscopy*, 48(9), 1222-1228.
- Eremets, M. I., Trojan, I. A., Medvedev, S. A., Tse, J. S., & Yao, Y. (2008). Superconductivity in hydrogen dominant materials: Silane, *Science*, 319(5869), 1506-1509.
- Flores-Livas, J. A., Sanna, A., Profeta, G., Arita, R., Eremets, M. (2020). A perspective on conventional high-temperature superconductors at high pressure: Methods and materials, *Physics Reports*, 856, 1-78.
- Drozdov, A. P., Kong, P. P., Minkov, V. S., Besedin, S. P., Kuzovnikov, M. A., Mozaffari, S., Balicas, L., Balakirev, F. F., Graf, D. E., Prakapenka, V. B., Greenberg, E., Knyazev, D. A., Tkacz, M., & Eremets, M. I. (2019). Superconductivity at 250 K in lanthanum hydride under high pressures, *Nature*, 569, 528-540.
- Duan, D., Yu, H., Xie, H., & Cui, T. (2019). Ab initio approach and its impact on superconductivity, *Journal of Superconductivity and Novel Magnetism*, 32, 53-60.
- Davydov, A., Sanna, A., Pellegrini, C., Dewhurst, J. K., Sharma, S., & Gross, E. K. U. (2020). Ab initio theory of plasmonic superconductivity within the Eliashberg and density-functional formalisms, *Physical Review B*, 102, 214508.
- Ohgoe, T., Hirayama, M., Misawa, T., Ido, K., Yamaji, Y., & Imada, M. (2020). Ab initio study of superconductivity and inhomogeneity in a Hg-based cuprate superconductor, *Physical Review B*, 101, 045124.
- Oganov, A.R., & Glass, C.W. (2006). Crystal structure prediction using evolutionary algorithms: principles and applications, *The Journal of Chemical Physics*, 124(24), 244704.
- Oganov, A.R., Stokes, H., & Valle, M. (2011). How evolutionary crystal structure prediction works and why, *Accounts of Chemical Research*, 44(3), 227-237.
- Lyakhov, A.O., Oganov, A.R., Stokes, H., & Zhu, Q. (2013). New developments in evolutionary structure prediction algorithm USPEX, *Computer Physics Communications*, 184, 1172-1182.
- Chou, C. Y., Kim, H., & Hwang, G. S. (2011). A comparative first-principles study of the structure, energetics, and properties of Li-M (M = Si, Ge, Sn), alloys. *The Journal of Physical Chemistry C*, 115, 20018-20026.
- Na, S. H., & Park, C. H. (2010). First-principles study of the structural phase transition in Sn. *Journal of the Korean Physical Society*, 56(1(2)), 494-497.
- Hohenberg, P., & Kohn, W. (1964). Inhomogeneous electron gas, *Physical Review Journals Achieve*, 136(3B), B864-B871.



23. Gonze, X., Ghosez, Ph., & Godby, R.W. (1997). Density functional theory of polar insulators. *Physical Review Letters*, 27(2), 294-297.
24. Kresse, G., & Furthmüller, J. (1996). Efficient iterative schemes for ab initio total-energy calculations using a plane-wave basis set. *Physical Review B Condensed Matter*, 54(16), 11169-11186.
25. Kresse, G., & Furthmüller, J. (1996). Efficiency of ab-initio total energy calculations for metals and semiconductors using a plane-wave basis set, *Computational Materials Science*, 6(1), 15-50.
26. Perdew, J., & Wang, Y. (1992). Accurate and simple analytic representation of the electron-gas correlation energy, *Physical Review B*, 45(23), 13244-13249.
27. Hamann, D. R., Wu, X., Rabe, K. M., & Vanderbilt, D. (2005). Metric tensor formulation of strain in density-functional perturbation theory, *Physical Review B*, 71(3), 035117-035129.
28. Gonze, X., Rignanese, G.-M., Verstraete, M., Beuken, J.-M., Pouillon, Y., Caracas, R., Jollet, F., Torrent, M., Zerah, G., Mikami, M., Ghosez, Ph., Veithen, M., Raty, J.-Y., Olevano, V., Bruneval, F., Reining, L., Godby, R., Onida, G., Hamann, D.R., & Allan, D.C. (2005). A brief introduction to the ABINIT software package, *Zeitschrift für Kristallographie-Crystalline Materials*, 220, 558-562.
29. Gonze, X., Amadon, B., Anglade, P.-M., Beuken, J.-M., Bottin, F., Boulanger, P., Bruneval, F., Caliste, D., Caracas, R., Cote, M., Deutsch, T., Genovese, L., Ghosez, Ph., Giantomassi, M., Goedecker, S., Hamann, D.R., Hermet, P., Jollet, F., Jomard, G., Leroux, S., Mancini, M., Mazevet, S., Oliveira, M.J.T., Onida, G., Pouillon, Y., Rangel, T., Rignanese, G.M., Sangalli, D., Shaltaf, R., Torrent, M., Verstraete, M.J., Zerah, G., & Zwanziger, J.W. (2009). ABINIT: First-principles approach of materials and nanosystem properties. *Computer Physics Communications*, 180(12), 2582-2615.
30. Perdew, J. P., Burke, K., & Ernzerhof, M. (1996). Generalized gradient approximation made simple. *Physical Review Letters*, 77(18), 3865-3868.
31. Olinger, B., & Shaner, W. (1983). Lithium, compression and high-pressure structure, *Science*, 219(4588), 1071-1072.
32. Hanfland, M., Loa, I., Syassen, K., Schwarz, U., & Takemura, K. (1999). Equation of state of lithium to 21 GPa, *Solid State Communications*, 112(3), 123-127.
33. Struzhkin, V. V., Hemley, R. J., & Mao, H. K. (1999). Compression of lithium to 120 GPa, *Bulletin of the American Physical Society*, 44, 1489-1499.
34. Bennett Dean, J., Vern, B. E., & Hall, T. (1963). X-ray diffraction studies on tin to 100 kilobars, *Journal of Applied Physics*, 37(2), 875-877.
35. Olijnyk, H., & Holzapfel, W. (1984). Phase transitions in Si, Ge and Sn under pressure, *Journal de Physique Colloques*, 45(C8), 153-156.
36. Liu, M., & Liu, L. (1986). Compressions and phase transitions of tin of half a megabar, *High Temperatures-High Pressures*, 18, 79-85.
37. Mouhat, F., & Coudert, F. X. (2014). Necessary and sufficient elastic stability conditions in various crystal systems, *Physical Review B*, 90(22), 224104.
38. Sin'ko, G. V., & Smirnov, N. A. (2005). Relative stability and elastic properties of hcp, bcc, and fcc beryllium under pressure, *Physical Review B*, 71(21), 214108.
39. McMillan, W. (1968). Transition temperature of strong-coupled superconductors, *Physical Review*, 167, 331.
40. Eliashberg, G. M. (1960). Interactions between electrons and lattice vibrations in a superconductor, *Journal of Experimental and Theoretical Physics*, 38, 966.
41. Frohlich, H. (1950). Theory of the superconducting state. I. The ground state at the absolute zero of temperature, *Physical Review*, 79(5), 845-856.
42. Allen, P. B., & Dynes, R. (1975). Transition temperature of strong-coupled superconductors reanalyzed, *Physical Review B*, 12, 905.
43. Morel, P., & Anderson, P. W. (1962). Calculation of the superconducting state parameters with retarded electron-phonon interaction, *Physical Review*, 125, 1263.
44. Mitrović, B., Zarate, H. G., & Carbotte, J. P. (1984). The ratio  $2\Delta(0)/k_B T_c$  within Eliashberg theory, *Physical Review B*, 29(1), 184-190.